



# Improved passivation and anticorrosion behaviors of selective laser melted Inconel 718 alloy in acidic solutions

Yanxin Qiao<sup>1</sup> · Wentao Zhang<sup>1</sup> · Najla AlMasoud<sup>2</sup> · Xinwang Shen<sup>1</sup> · Shunli Zheng<sup>3</sup> · Taghrid S. Alomar<sup>2</sup> · Zeinhom M. El-Bahy<sup>4</sup> · Mohamed M. Ibrahim<sup>5</sup> · Hassan Algadi<sup>6</sup> · Wen Liu<sup>1</sup>

Received: 9 July 2023 / Revised: 26 October 2023 / Accepted: 2 November 2023 / Published online: 11 November 2023  
© The Author(s), under exclusive licence to Springer Nature Switzerland AG 2023

## Abstract

The electrochemical behaviors of Inconel 718 alloy prepared by selective laser melting (SLM) were investigated and compared with commercial rolled counterpart in 0.05 mol/L H<sub>2</sub>SO<sub>4</sub> solution. For this purpose, open circuit potential (OCP), electrochemical impedance spectroscopy (EIS), potentiodynamic polarization, scanning electron microscopy (SEM), transmission electron microscopy (TEM), and X-ray photoelectron spectroscopy (XPS) analyses were performed. The corrosion resistance of selective laser melted (SLMed) Inconel 718 alloy is superior to that of the rolled counterpart, which can be attributed to the difference in the microstructure and the chemical compositions of the passive film. The SLMed 718 alloy suffers from severely localized corrosion due to the micro-galvanic corrosion induced by the Laves phase. Furthermore, compared with the rolled counterpart, the passive film formed on SLMed 718 alloy has more content of Cr<sub>2</sub>O<sub>3</sub> and less content of NiO. The significance of this study laid in the understanding of the corrosion behavior of Inconel 718 alloy prepared by SLM. These findings aided in the development of strategies to further enhance the corrosion resistance and overall performance of this alloy in various applications.

**Keywords** Corrosion · Selective laser melting · Inconel 718 alloy · Passive film

## 1 Introduction

Metals, alloys and their composites especially at the nanoscale have been well studied experimentally and theoretically due to their wide applications [1–9]. Methods to process and manufacture them have been developed [10–14]. Additive manufacturing (AM) has attracted considerable attention due to the relatively low costs and high efficiency [15]. AM technologies such as direct laser deposition (DLD) [16–18], electron beam melting (EBM) [19], wire arc additive manufacturing (WAAM) [20], and selective laser melting (SLM) [21], electrospinning [22, 23] have been employed to fabricate polymers, metallic/polymer composites, metallic materials and advanced alloys. Due to the special forming process, the microstructure and composition distribution of additively manufactured (AMed) materials are different from that of their counterparts fabricated by traditional fabrication techniques, resulting in different corrosion behaviors.

Corrosion resistance is one of the most important considerations in the use of AMed metallic materials [24]. AM process can alter the stability of the passive film of nickel-based

✉ Yanxin Qiao  
yxqiao@just.edu.cn

✉ Shunli Zheng  
zhengshunli1986@126.com

<sup>1</sup> School of Materials Science and Engineering, Jiangsu University of Science and Technology, Zhenjiang 212100, China

<sup>2</sup> Department of Chemistry, College of Science, Princess Nourah Bint Abdulrahman University, P.O. Box 84428, Riyadh 11671, Saudi Arabia

<sup>3</sup> College & Hospital of Stomatology, Key Lab. of Oral Diseases Research of Anhui Province, Anhui Medical University, Hefei 230032, China

<sup>4</sup> Department of Chemistry, Faculty of Science, Al-Azhar University, Nasr City, Cairo 11884, Egypt

<sup>5</sup> Department of Chemistry, College of Science, Taif University, P.O. Box 11099, Taif 21944, Saudi Arabia

<sup>6</sup> Department of Electrical Engineering, Faculty of Engineering, Najran University, Najran 11001, Saudi Arabia

alloys [25] titanium alloys [26], and stainless steels [27]. Pütz et al. [20] found that the corrosion properties of WAAMed functionally graded materials (FGM) are determined by the micro-galvanic coupling and chemical composition of the various phases. Zhang and Ojo [25] found that the corrosion performance of WAAMed Inconel 718 was inferior to that of its wrought counterpart in 1 mol/L  $H_2SO_4$ . The corrosion resistance of SLMed Ti-6Al-4 V (wt.% in the present article) alloy deteriorates with the increase of laser scan speed, which can be attributed to the decreased densification and increased micropores [28]. The corrosion resistance of EBMed Ti-6Al-4 V alloy is slightly higher than that of its wrought counterpart in phosphate buffered saline because of the ultrafine-grained lamellar  $\alpha/\beta$  phases and larger proportions of  $\beta$  phase [29]. Kong et al. [27] reported that SLMed 316L SS exhibits higher corrosion resistance than wrought 316L SS, which is attributed to the rapid formation of a thicker passive film. High-density sub-grain boundaries in the SLMed 316L SS provide nucleation sites for oxide film. In addition, the micro-galvanic couples accelerate the formation of oxide film. Dai et al. [30] reported that the corrosion resistance of SLMed Ti-6Al-4 V is inferior to that of commercial Grade 5 alloy owing to the high fraction of acicular  $\alpha'$  phase and lower fraction of  $\beta$ -Ti phase. In the investigation on the electrochemical corrosion of different phases of laser solid formed Inconel 718 in  $NaNO_3$  solution, Guo et al. [31] found that Nb-rich  $\gamma$  phase dissolves faster than  $\gamma$  matrix due to its higher lattice distortion energy, lower corrosion potential, and higher free energy of atoms on the phase boundaries.

Inconel 718 alloy is extensively applied in aerospace, nuclear, oil, and gas industries due to its exceedingly superior mechanical properties, excellent oxidation resistance, corrosion resistance, and environmentally assisted cracking resistance [31]. Although the microstructure and mechanical properties of SLMed Inconel 718 alloy have been investigated in details, its corrosion resistance, particularly in oil-field upstream environments, has received rare attention. The corrosion resistance of SLMed 718 alloy in 0.1 mol/L NaOH solution is better than that of R (rolled) 718 alloy [32]. In contrast, when the corrosive medium changed to 3.5 wt. % NaCl solution, SLMed 718 alloy exhibits poorer corrosion resistance than that of R 718 alloy [33]. The corrosion resistance of SLMed 718 alloy in 3.5 wt.% NaCl solution can be enhanced by appropriate heat treatment through reducing micro-segregation and modifying second phase morphology. However, the corrosion resistance of SLMed 718 alloy is still inferior to that of R Inconel 718 alloy [33]. Du et al. [34] revealed that

building orientation exerts an effect on the corrosion resistance of SLMed Inconel 718 alloy through affecting crystallographic texture and grain boundary density. In the study on the corrosion behavior of LDEDed Inconel 718 alloy in different acidic environments (i.e., HCl,  $H_2SO_4$ , and  $HNO_3$ ), Guo et al. [35] found that high-deposition-rate laser solid formed Alloy 718 exhibits electrochemical activity isotropy in 10 wt.%  $NaNO_3$  solution due to the formation of an amorphous bilayer passive film. In reviewing the published literatures, an interesting but consistent phenomenon concerning the corrosion properties of AMed metallic alloys in various corrosive solutions emerged. Many researchers have focused on fabricating Inconel 718 alloy using SLM in recent decades [33, 36, 37], but rare attention has been paid to its corrosion and passivity behaviors in highly corrosive aqueous environments.

In this work, potentiodynamic polarization, electrochemical impedance spectroscopy (EIS), scanning electron microscopy (SEM) and X-ray photoelectron spectroscopy (XPS) were employed to investigate the corrosion behavior of SLMed 718 alloy and its commercial rolled counterpart in 0.05 mol/L  $H_2SO_4$  solution. In the end, their underlying corrosion mechanisms were unveiled.

## 2 Experimental

### 2.1 Materials

The Inconel 718 alloy used in the present work was prepared by SLM (SLMed 718 alloy), and the commercial rolled Inconel 718 alloy (R 718 alloy) was used for comparison. The chemical compositions of SLMed 718 and R 718 alloys are shown in Table 1. The samples were sealed in a mixture of epoxy and polyamide resins, then ground with SiC abrasive papers up to 1200 grit, cleaned in ethanol, and finally dried in hot air. An interface 1010E electrochemical workstation (Gamry Instruments) was used to evaluate the electrochemical response of the samples. Typical three-electrode cells were constructed, with a test sample as the working electrode, a platinum with a surface area of  $30\text{ cm}^2$  as the counter electrode, and a saturated calomel electrode (SCE) as the reference electrode. The electrolyte used in this work was 0.05 mol/L  $H_2SO_4$  solution at the temperature of  $25 \pm 1\text{ }^\circ\text{C}$ .

Open circuit potential (OCP) was measured and recorded for one h to attain a relatively stable state. Potentiodynamic polarization tests were conducted from 500 mV below OCP,

**Table 1** Chemical compositions of SLMed 718 and R 718 alloys (%)

	Ni	Cr	Nb	Mo	Ti	Al	Co	Cu	Mn	Fe
<b>SLM 718</b>	52.53	19.00	5.10	3.02	0.96	0.48	0.031	0.035	0.074	Bal.
<b>R 718</b>	53.20	19.20	5.10	3.10	0.90	0.30	0.85	0.25	0.29	Bal.

with a scanning rate of 10 mV/min and a current density limit of 10 mA/cm<sup>2</sup>. The specimens were immersed in the test solution for up to 168 h with record of OCP and electrochemical impedance spectroscopy (EIS) results every 24 h for the specimens. The EIS measurements were performed at an amplitude of the sinusoidal signal of 10 mV with a frequency range of 10<sup>4</sup> ~ 10<sup>-2</sup> Hz. All electrochemical tests were repeated at least three times to ensure repeatability.

The corrosion morphologies of the specimens after potentiodynamic polarization test were observed under scanning electron microscope (SEM). The passive film was formed on the specimen surface after immersion in the test solution for 24 h, 72 h, 120 h and 168 h. The chemical composition of the passive film was analyzed by X-ray photoelectron spectroscopy (XPS, Thermo Scientific Nexsa) with a AlK<sub>α</sub> (1486.6 eV) radiation source, and the high-resolution spectra of Ni 2p, Fe 2p, Cr 2p and O1s were recorded and the binding energy of C1s peak was calibrated at 248.8 eV. The surface was sputtered by argon ion bombardment with an ion beam of 1 kV to obtain depth profiles. All XPS data were analyzed using Thermo Avantage software.

The microstructure of SLMed and R 718 alloys was characterized using optical microscopy (OM, Olympus BX51M), scanning electron microscopy (SEM, Leo 1530 VP), and transmission electron microscopy (TEM, FEI, Talos F200X) equipped with energy-dispersive X-ray spectroscopy (EDS). The microstructure of SLM-USSR was examined by TEM (FEI, Talos F200X) with EDS. The surface topography and Volta potential (the contact potential difference between the probe and the sample through equilibrium potential) were acquired using a Dimension Icon atomic force microscopy (AFM, Bruker Corporation, CA, USA) equipped with scanning Kelvin probe force microscopy (SKPFM). The selected area on the sample surface was scanned at ambient temperature in air using Peak Force KPFM-AM mode with Nano-probe™ SCM-PIT probe (Bruker, USA) at a scan rate of 0.5

Hz. A dual-scan mode was used to record a second signal in addition to the surface topography signal. The specimens for OM, SEM and SKPFM were prepared by grinding and mechanically polishing followed by electrochemically polishing in the 10% oxalic acid aqueous solution. TEM images were acquired from the topmost surface layer at a depth of ~1 mm of samples, and the samples were prepared by milling with a single-side ion milling instrument (Gatan, PIPS II 695).

## 3 Results and discussion

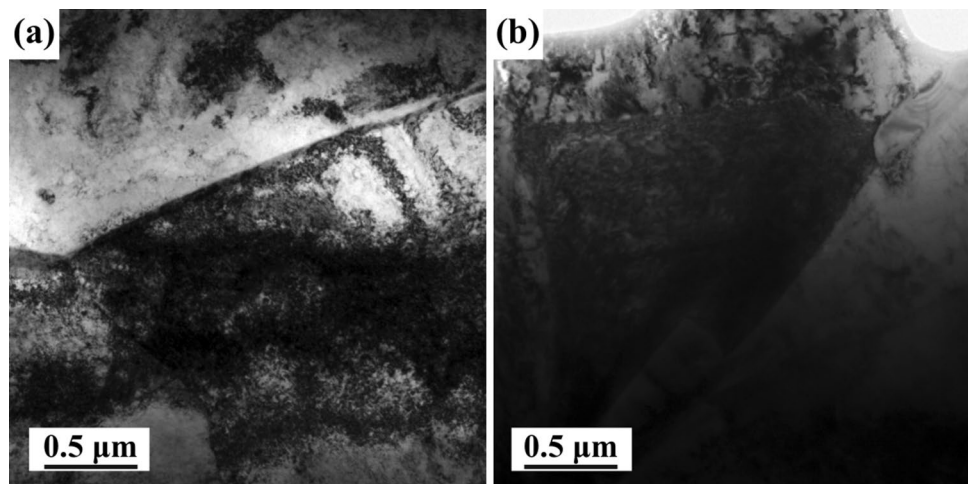
### 3.1 Microstructural characterization

Figure 1 shows the TEM microstructure of the SLMed 718 and R 718 alloys. Due to the formation of thermal stress during the SLM alloy preparation process, the samples will deform and the grains formed at the grain boundaries hinder the movement of dislocations, forming a dislocation entanglement. At the same time, a large number of dislocations accumulate at the grain boundaries, resulting in a high dislocation density, which indicating the higher internal stress. The dislocations exhibit dislocation cell type, indicating that the higher stacking fault energy of SLMed 718 alloy. As shown in Fig. 1(b), it can be seen that the formation positions of the carbides (i.e., NbC or M<sub>23</sub>C<sub>6</sub>) commonly precipitate along the grain boundaries.

### 3.2 Potentiodynamic polarization

Figure 2 shows the potentiodynamic polarization curves of SLMed 718 and R 718 alloys in 0.05 mol/L H<sub>2</sub>SO<sub>4</sub> solution. Figure 3 illustrates the SEM observation of the corresponding corroded surface. The two polarization curves are roughly the same except for the corrosion potential

**Fig. 1** TEM of the two tested 718 alloys: **a** SLMed 718, **b** R 718 alloy



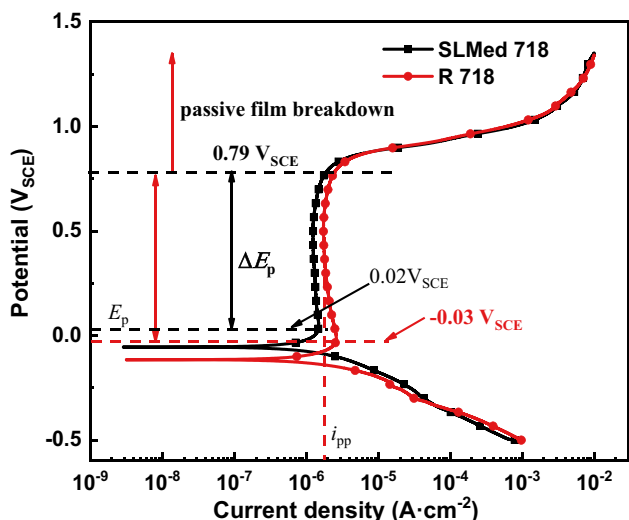
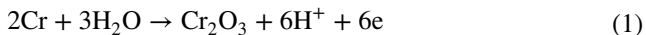
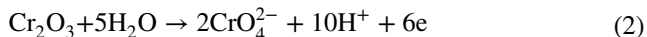


**Fig. 2** Potentiodynamic polarization curves of SLMed 718 and R 718 alloys in 0.05 mol/L H<sub>2</sub>SO<sub>4</sub> solution

( $E_{corr}$ ). The cathodic branches are the hydrogen evolution reactions (HER) in H<sub>2</sub>SO<sub>4</sub> solution, and the anodic branches exhibits a typical active-to-passive behavior [25, 27]. No obvious pitting corrosion is observed in Fig. 2. The passivation of these two alloys is caused by the formation of a Cr<sub>2</sub>O<sub>3</sub>-dominated passive film as presented by Eq. (1):



The current density of the two alloys at potential higher than 0.79 V<sub>SCE</sub>, increasing rapidly mainly due to the dissolution of the passive film, rather than oxygen evolution reaction in H<sub>2</sub>SO<sub>4</sub> solution [38]. Similar degradation potentials of both alloys indicate that the breakdown of the passive film is not resulted from the localized corrosion, which is attributed to the oxidation of Cr<sub>2</sub>O<sub>3</sub> to the more soluble CrO<sub>4</sub><sup>2-</sup> [39]:



The passive performance of materials is closely related to electrochemical parameters, such as passive potential ( $E_p$ ), passive current density ( $i_p$ ) and passive range ( $\Delta E_p$ ) [29, 40]. Table 2 presents the electrochemical parameters derived from Fig. 2. The similar passive range ( $\Delta E_p$ ) and trend in passive region suggest that the passive films of the two alloys may possess analogous structure [41]. Corrosion potential of R 718 alloy is -117.31 mV<sub>SCE</sub>, lower than that of SLMed 718 alloy (-52.63 mV<sub>SCE</sub>), indicating a better thermodynamic stability. The corrosion current density of R 718 alloy ( $3.30 \times 10^{-6}$  A·cm<sup>-2</sup>) is higher than that of SLMed 718 alloy ( $1.91 \times 10^{-6}$  A·cm<sup>-2</sup>). The current study corresponds well to the previous reports [27], suggesting that SLMed 718 alloy has a superior corrosion resistance. In the passive range, the current density is on the order of 10<sup>-6</sup> A·cm<sup>-2</sup>. It is obvious that the passive current density of R 718 alloy is slightly higher than that of SLMed 718 alloy, while the passive potential of R718 alloy is slightly lower than that of SLMed 718 alloy. The former characterization could be due

**Fig. 3** SEM images of the two tested alloys after potentiodynamic polarization test in 0.05 mol/L H<sub>2</sub>SO<sub>4</sub>: **a, b** SLMed 718 alloy, **c, d** R 718 alloy

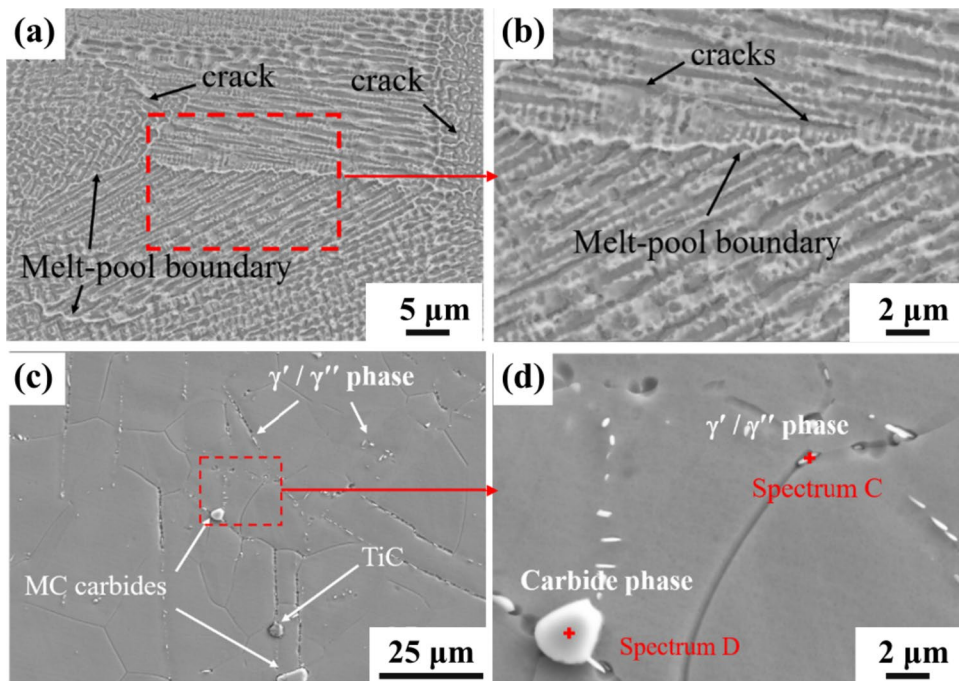




**Table 2** Electrochemical parameters of SLMed 718 and R 718 alloys derived from Fig. 2

	$E_{\text{corr}} / \text{mV}_{\text{SCE}}$	$i_{\text{corr}} / \text{A}\cdot\text{cm}^{-2}$	$i_p / \text{A}\cdot\text{cm}^{-2}$	$\Delta E_p / \text{mV}_{\text{SCE}}$
SLMed 718 alloy	$-52.63 \pm 1.80$	$(1.91 \pm 0.14) \times 10^{-6}$	$(1.34 \pm 0.06) \times 10^{-6}$	$653 \pm 7.00$
R 718 alloy	$-117.31 \pm 1.23$	$(3.30 \pm 0.05) \times 10^{-6}$	$(1.81 \pm 0.05) \times 10^{-6}$	$673 \pm 9.50$

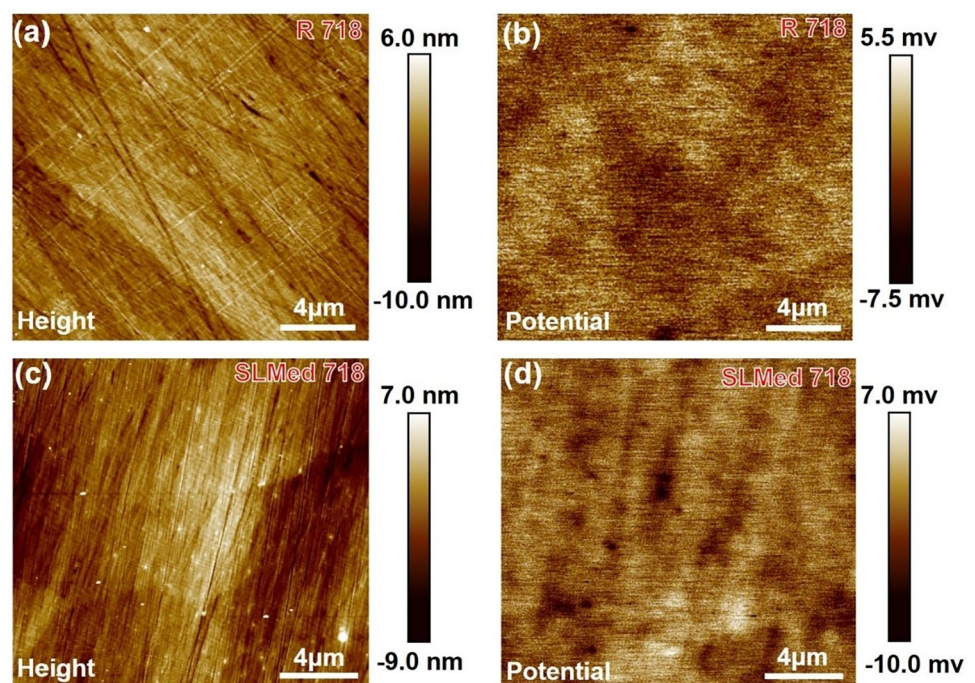
to the higher reactivity of the surface. SLMed 718 alloy has high-density sub-grain boundaries, which provide nucleation sites for the oxide film, as reported by Kong et al. [27]. The latter characterization could be attributed to the superior passivity of SLMed 718 alloy. Thus, it appears that the passive film formed on SLMed 718 alloy surface has better stability and protective properties.

Figure 3 shows the surface morphologies of SLMed and R 718 alloys after potentiodynamic polarization test. It is obvious that these two alloys suffered severely localized corrosion. SLMed 718 alloy exhibits the typical dendrite structure, which is similar to the micro-galvanic corrosion, as shown in Fig. 3(a). Figure 3(b) reveals that micro-galvanic corrosion appeared at the interfaces of dendrites, Laves phases and matrix. The Laves phase is Nb- and Mo-rich phase, depleted in Cr, Fe and Ni [31, 42]. The Laves phases and matrix act as cathode and anode respectively, forming micro-galvanic corrosion. The results agree well with the previous studies, which show similar segregation behaviors in laser solid formed (LSFed) Inconel 718 [31] and LDEDed Inconel 718 [43].

However, R 718 alloy suffered severely intergranular corrosion, as shown in Fig. 3(c). The magnified image in Fig. 3(d) reveals that the preferential corrosion occurred

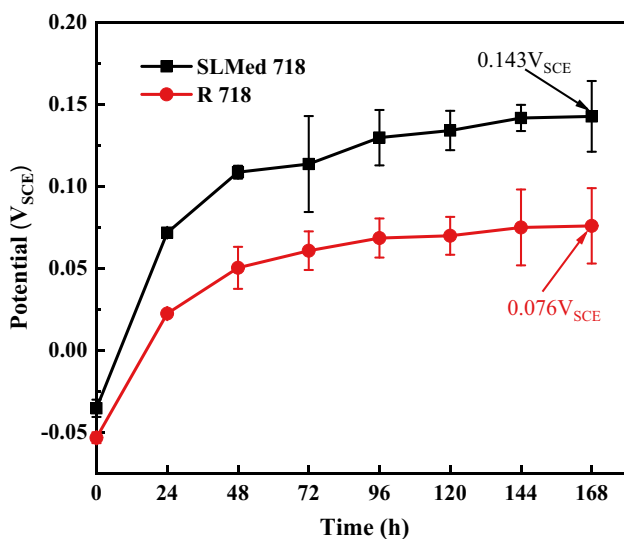
along the grain boundaries or around the  $\gamma'/\gamma''$  phases and undissolved NbC carbide phases. Interestingly, they were preserved and surrounded by micro-cracks. Similar corrosion morphologies were also observed in previous works [44, 45]. The micro-cracks may be induced by the serious lattice misfit or stress induced by the precipitation and  $\gamma$  matrix [44], thus accelerating the anodic dissolution. As a result, the passive film can easily break down at these sites, leading to the formation of micro-cracks.

Figure 4 presents the AFM/SKPFM images of the original sample surface before corrosion testing. It can be seen from Fig. 4(a) and (c) that the surfaces of both samples of R718 and SLMed 718 alloys are relatively flat. The Volta potential result shown in Fig. 4(b) implies no significant potential difference in this area, which is consistent with the microstructural characteristics of the single-phase austenite of sample R 718 alloy. However, the Volta potential map exhibited in Fig. 4(d) indicates that the introduction of second phases does not result in significant potential differences, which is usually associated with the local corrosion. This is in accordance with the electrochemical testing results. Furthermore, it can be deduced from this Volta potential result that the distribution of the second phases of SLMed 718 alloy is small and uniform.

**Fig. 4** Topographic maps and Volta potential maps of the two tested alloys: **a, b** R718 alloy and **c, d** SLMed 718 alloy

### 3.3 Open circuit potential (OCP)

The OCP curves of SLMed and R 718 alloys after immersion in 0.05 mol/L  $\text{H}_2\text{SO}_4$  solution for different time are shown in Fig. 5. It can be seen that the OCP of both alloys increases gradually to be positive, suggesting the formation of passive film on the sample surfaces. The phenomenon results from predominance of passivation during the corrosion process, suggesting that the samples are in a spontaneous passivation state. The OCP of the SLMed 718 alloy is always higher than that of the R 718 alloy, suggesting that SLM 718 alloy is less active and susceptible to corrosion [32]. The OCPs of SLMed 718 and R 718 alloys increase dramatically during the initial immersion period, which is associated with the competition between dissociation of oxide layer formed in air and formation of passive film in 0.05 mol/L  $\text{H}_2\text{SO}_4$  solution. A similar phenomenon was reported for passive materials such as Inconel alloy 718 [46], titanium and titanium alloys [47], as well as stainless steel [48, 49] in  $\text{H}_2\text{SO}_4$  solution. As the immersion time extends, the increasing trend of OCP slows down gradually, and OCP eventually reaches a steady value. Interestingly, the time for reaching steady state is different for the two alloys, i.e., 144 h for SLMed 718 alloy and 96 h for R 718 alloy, respectively. Dai et al. [30] reported that OCP of the commercial Ti-6Al-4 V (Grade 5) stabilizes after approximately 25 h, whereas SLMed Ti-6Al-4V stabilizes after 60 h. The stabilized potential of SLMed 718 alloy ( $0.143\text{V}_{\text{SCE}}$ ) exceeds that of R 718 alloy ( $0.076\text{V}_{\text{SCE}}$ ) by  $67\text{mV}_{\text{SCE}}$ . The high activity



**Fig. 5** OCP curves of SLMed 718 and R 718 alloys immersed in 0.05 mol/L  $\text{H}_2\text{SO}_4$  solution

of AMed metallic materials indicates the formation of stable passive film, which is in good agreement with previous findings [32, 50].

### 3.4 Electrochemical impedance spectroscopy (EIS)

Figure 6 presents the EIS of SLMed and R 718 alloys after immersion in 0.05 mol/L  $\text{H}_2\text{SO}_4$  solution for different time. It is found that Nyquist plots of the two alloys exhibit a similar shape of an incomplete semi-arc, showing a charge transfer process at the interface of electrode/solution, as shown in Fig. 6(a) and (c). The semicircular arcs of both alloys increase with the prolongation of immersion time, indicating the growth of passive film and enhancement in electrochemical characteristics [51, 52]. Obviously, the impedance value of SLMed 718 alloy is larger than that of R 718 alloy, implying the superior corrosion resistance of SLMed 718 alloy. Bode plots of both alloys are shown in Fig. 6(b) and (d). In the low frequency region, the initial impedance modulus ( $|Z|_{0.01\text{Hz}}$ ) of both alloys increases with prolong of the immersion time. In the meanwhile, the value of  $|Z|_{0.01\text{Hz}}$  retains unchangeable during a longer immersion time, implying the formation of relatively stable passive film. In the medium–low frequency range from approximately  $10^{-1}$  to  $10^2$  Hz, the phase angle approaches  $-80^\circ$ , indicating the formation of stable passive film. In particular, the maximum phase angle of SLMed 718 alloy shifts to low frequency with increasing the immersion time, implying the optimization of the corrosion resistance of the passive film [53, 54].

Figure 7 shows the equivalent electrical circuit of the EIS results. The constant phase element (CPE), instead of the capacitance, was used due to the heterogeneity of electrode surfaces [40, 55]. The symbols, such as  $R_s$  is solution resistance,  $R_{f1}$  is the resistance of the passive film, and  $C_{f2}$  and  $R_{f2}$  are capacitance of the electric double layer and charge-transfer resistance of the Faraday processes, respectively [52]. Table 3 shows the fitted results of the EIS data for SLMed 718 and R 718 alloys. The fitted data is in good agreement with the experimental data. As the immersion time prolongs,  $R_{f2}$  and  $R_{f1}$  increase, whereas  $Q_{f1}$  decreases, implying the defect reduction in the passive film and strong resistance of the passive film to charging and ion transferring.

Polarization resistance ( $R_p$ ,  $R_p = R_{f1} + R_{f2}$ ) is usually used to assess the corrosion properties of metallic materials. In the immersion initial stage (0 h),  $R_p$  values for the two alloys are  $1.98 \times 10^5 \Omega \cdot \text{cm}^2$  and  $1.38 \times 10^5 \Omega \cdot \text{cm}^2$ , respectively. With prolonging the immersion time,  $R_p$  rises substantially. When the immersion time reaches 168 h,  $R_p$  increases by nearly two orders of magnitude. Noticeably,  $R_p$  of SLMed 718 alloy is always higher than that of R 718 alloy, indicating much more excellent corrosion resistance of SLMed 718 alloy. The thickness of the passive film can be estimated using Eqs. (3) and (4) [51]:

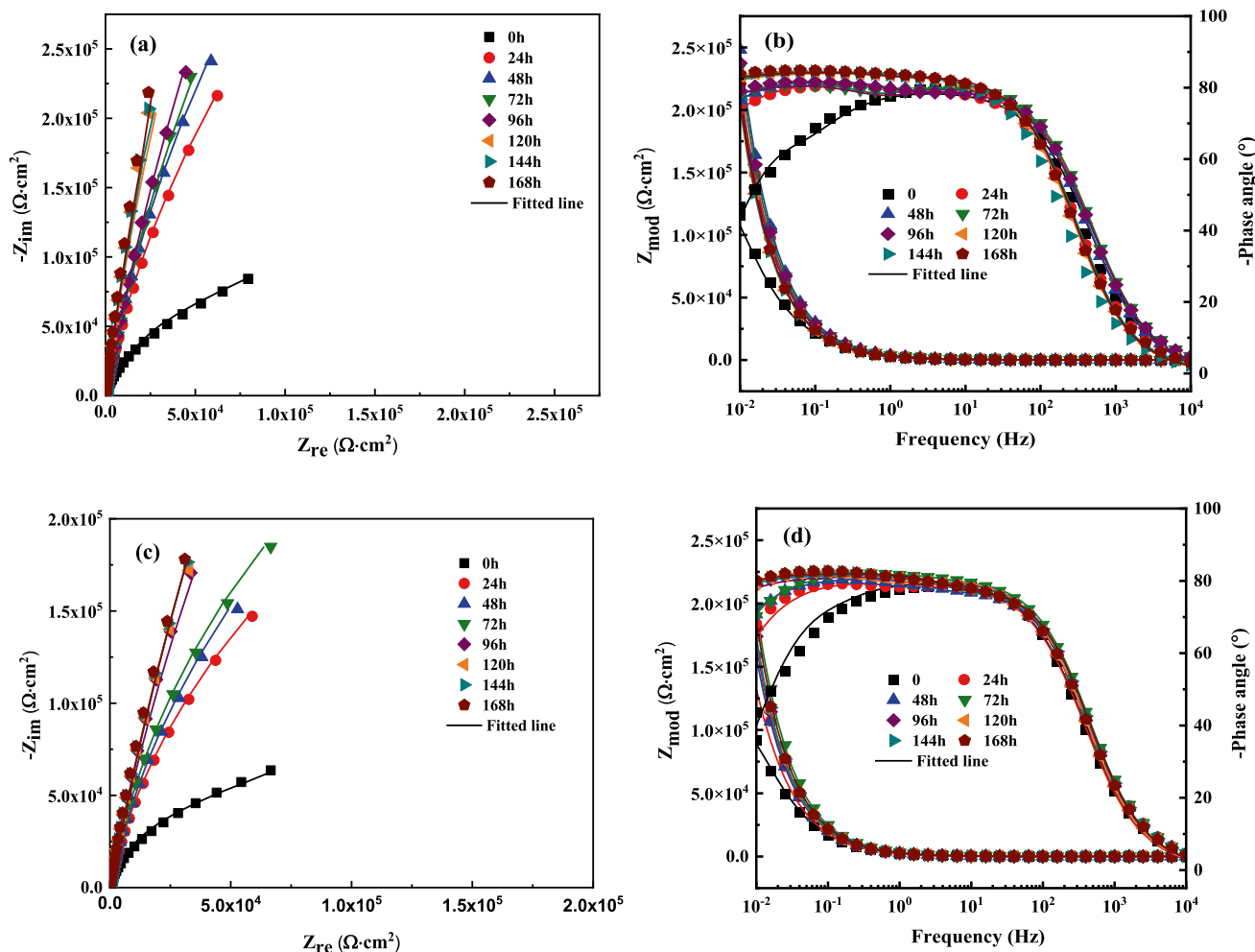


Fig. 6 EIS of the two tested alloys after immersion in 0.05 mol/L H<sub>2</sub>SO<sub>4</sub> solution for different time: **a** Nyquist, **b** Bode plots of SLMed 718 alloy; **c** Nyquist, **d** Bode plots of R 718 alloy

$$C_f = Q_n^{1/n} \cdot R_p^{(1-n)/n} \tag{3}$$

$$d = \frac{\epsilon \epsilon_0 A}{C_f} \tag{4}$$

where  $d$  is the thickness of passive film,  $\epsilon$  is the dielectric constant of the passive film,  $\epsilon_0$  is the vacuum permittivity constant ( $8.8542 \times 10^{-14}$  F·cm<sup>-1</sup>),  $A$  is the electrode

surface area (0.785 cm<sup>2</sup>), and  $C_f$  is capacitance of passive film. Although the dielectric constant of the passive film cannot be accurately obtained, the thickness of the passive film is inversely proportional to the capacitance. Thus, the decrease of  $C_f$  with the increase of immersion time indicates the increase of passive film thickness. The passive film of the SLMed 718 alloy is thicker than that of the R 718 alloy, as indicated by its slightly lower  $C_f$ . Thus, the passive film of the SLMed 718 alloy has stronger protective ability than

Fig. 7 Schematic of equivalent circuit modeling of EIS

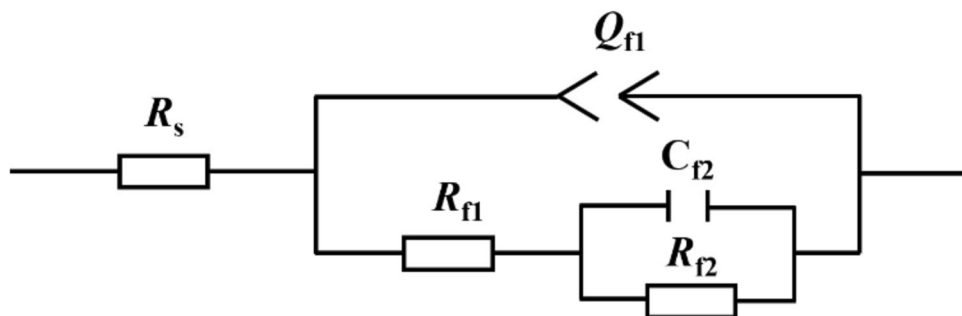


**Table 3** Electrical parameters obtained by fitting EIS data of SLMed 718 and R 718 alloys

	Time /h	$R_s$ / $\Omega \cdot \text{cm}^2$	$Q_{r1}$ / $\Omega^{-1} \cdot \text{cm}^{-2} \cdot \text{s}^{-n}$	$n$	$R_{r1}$ / $\Omega \cdot \text{cm}^2$	$C_{r2}$ / $F \cdot \text{cm}^{-2}$	$R_{r2}$ / $\Omega \cdot \text{cm}^2$
SLMed 718 alloy	0	14.05	$5.92 \times 10^{-5}$	0.89	$9.8 \times 10^4$	$8.95 \times 10^{-6}$	$1.0 \times 10^5$
	24	14.34	$5.18 \times 10^{-5}$	0.90	$9.90 \times 10^4$	$3.10 \times 10^{-6}$	$1.53 \times 10^6$
	48	13.49	$4.98 \times 10^{-5}$	0.88	$1.25 \times 10^5$	$3.67 \times 10^{-6}$	$2.38 \times 10^6$
	72	13.90	$4.73 \times 10^{-5}$	0.91	$1.47 \times 10^5$	$6.11 \times 10^{-6}$	$2.93 \times 10^6$
	96	13.65	$4.66 \times 10^{-5}$	0.92	$1.52 \times 10^5$	$3.74 \times 10^{-6}$	$4.87 \times 10^6$
	120	14.40	$4.40 \times 10^{-5}$	0.98	$2.32 \times 10^5$	$1.80 \times 10^{-6}$	$5.65 \times 10^6$
	144	14.04	$4.03 \times 10^{-5}$	0.99	$3.84 \times 10^5$	$4.72 \times 10^{-6}$	$6.26 \times 10^6$
	168	13.84	$3.80 \times 10^{-5}$	0.99	$5.53 \times 10^5$	$4.03 \times 10^{-6}$	$8.18 \times 10^6$
R 718 alloy	0	11.34	$8.66 \times 10^{-5}$	0.88	$4.82 \times 10^5$	$3.54 \times 10^{-6}$	$9.00 \times 10^4$
	24	11.96	$8.31 \times 10^{-5}$	0.90	$5.63 \times 10^5$	$2.04 \times 10^{-6}$	$3.60 \times 10^5$
	48	11.92	$7.86 \times 10^{-5}$	0.89	$6.91 \times 10^5$	$2.88 \times 10^{-6}$	$5.30 \times 10^5$
	72	11.82	$6.83 \times 10^{-5}$	0.90	$7.31 \times 10^5$	$2.06 \times 10^{-6}$	$6.10 \times 10^5$
	96	11.76	$6.59 \times 10^{-5}$	0.92	$9.94 \times 10^5$	$5.49 \times 10^{-6}$	$2.67 \times 10^6$
	120	11.91	$6.10 \times 10^{-5}$	0.91	$9.72 \times 10^5$	$4.21 \times 10^{-6}$	$5.15 \times 10^6$
	144	11.40	$5.65 \times 10^{-5}$	0.93	$9.87 \times 10^5$	$4.47 \times 10^{-6}$	$5.58 \times 10^6$
	168	11.87	$5.01 \times 10^{-5}$	0.94	$9.98 \times 10^5$	$4.56 \times 10^{-6}$	$7.33 \times 10^6$

that of the R 718 alloy. The larger imaginary component indicates an enhanced capacitance characteristic of the film which contributes to the improved protective ability.

### 3.5 XPS analysis

Figure 8 displayed the XPS spectra of Ni 2p, Fe 2p and Cr 2p of the passive film formed after deconvolution. It can be observed that the XPS spectra of Ni 2p, Fe 2p and Cr 2p were deconvoluted to two constituents of the metallic and oxidized states, reflecting that the main components of passive film were  $\text{Cr}_2\text{O}_3$ , NiO and  $\text{Fe}_2\text{O}_3$ . The XPS spectra of Ni 2p record Ni  $2p_{3/2}$  and Ni  $2p_{1/2}$ , which are mainly separated into several constituents of the metallic Ni, NiO and satellite peaks (SAT). The peak positions for Ni  $2p_{3/2}$  (Ni), Ni $2p_{1/2}$  (Ni), Ni $2p_{3/2}$  (NiO), Ni $2p_{1/2}$  (NiO), Ni $2p_{3/2}$  (SAT), and Ni $2p_{1/2}$  (SAT) are 852.6 eV, 869.9 eV, 855.2 eV, 872.8 eV, 860.7 eV, and 875.2 eV, respectively [33, 56, 57]. It is well-known that oxide species play an important role in the properties of passive film. The peak area ratio of NiO decreases with the increase of immersion time, indicating the reduction of NiO in the passive film. The XPS spectra of Fe 2p are divided into the metallic Fe (706.8 eV) and  $\text{Fe}_2\text{O}_3$  (711.3 eV). According to the previous studies [25, 58], the  $\text{Fe}_2\text{O}_3$  film was also detected in passive films of AMed 718 alloy. The XPS spectra of Cr 2p is deconvoluted to the metallic Cr (573.6 eV for Cr  $2p_{3/2}$  and 582.8 eV for Cr  $2p_{1/2}$ ) and  $\text{Cr}_2\text{O}_3$  (576.6 eV for Cr  $2p_{3/2}$  and 586.3 eV for Cr  $2p_{1/2}$ ). In the initial immersion stage, the intensity of  $\text{Cr}_2\text{O}_3$  is slightly

lower than that of Cr. With the immersion time extending, the intensity and percentage of  $\text{Cr}_2\text{O}_3$  increase from the transformation of Cr.

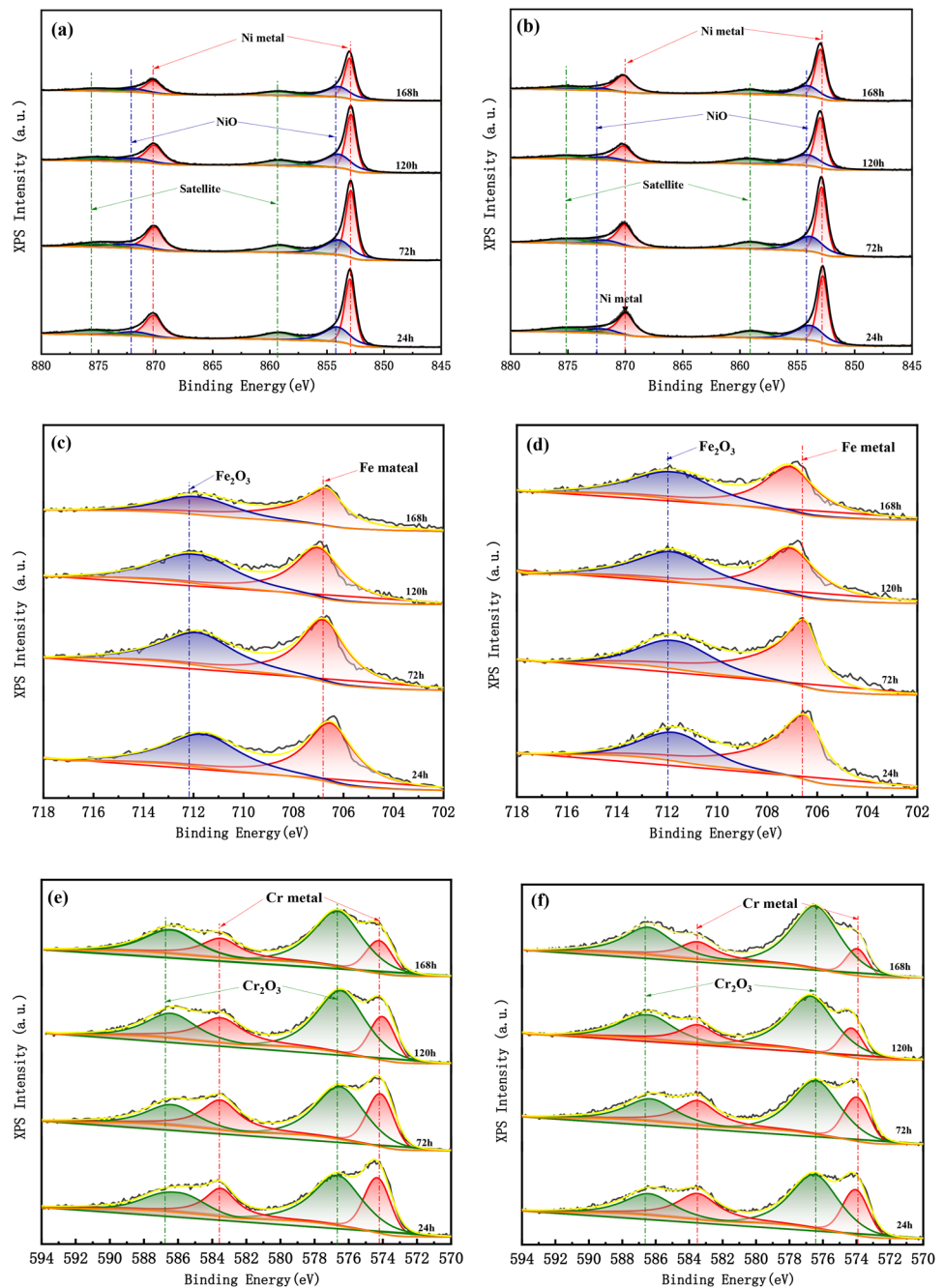
XPS analyses were conducted to determine the variation in film composition with depth. Figure 9 presents the depth distribution of elements in passive films on SLMed and R 718 alloys after immersion in 0.05 mol/L  $\text{H}_2\text{SO}_4$  solution for different time. The film composition analysis indicates that the passive corrosion behavior of Nickel-Based Alloys is primarily controlled by the presence of Cr, which can form a layer of  $\text{Cr}_2\text{O}_3$  film to protect the surface.

It can be observed that the O content decreases significantly and the Ni content increases in the passive film with increasing sputtering time, which indicates that the passive film is consumed and oxide species are gradually converted to metals for all cases. Fe is depleted in the outer layer of the passive film. Cr is usually enriched in the inner layer of the passive film [24, 46]. Due to the preferential dissolution of Fe in the acidic environment, the passive film changes from a Cr-rich inner layer to a Cr-rich outer layer [58, 59]. Furthermore, the Cr content first increases and then decreases with increasing sputtering time until reaching a steady value. This indicates that Cr is more easily enriched in the subsurface layer. Meanwhile, the Cr content first increases and then decreases slowly with increasing immersion time, indirectly evidencing that the passive film is thicker and more compact.

The percentages of different components in the passive film were calculated by normalization, as shown in Fig. 10. The main components of the passive film for SLMed alloys are NiO,  $\text{Cr}_2\text{O}_3$  and  $\text{Fe}_2\text{O}_3$ , which are consistent with the



**Fig. 8** Detailed XPS spectra of Ni 2p, Fe 2p and Cr 2p of the passive film formed on SLMed 718 alloy (a), (c), (e) and R 718 alloy (b), (d), (f)



previous reports [25]. The  $\text{Cr}_2\text{O}_3$  content in the passive film increases significantly, whereas the NiO content decreases with increasing immersion time. Since the  $\text{Cr}_2\text{O}_3$  is compact while the NiO is porous, the passive film of SLMed 718 alloy becomes more compact and protective with increasing immersion time. Moreover, with the prolongation of immersion time, the passive films of SLMed 718 alloy gradually thicken, and their ability to block corrosive medium becomes stronger, resulting in an enhanced protective ability.

### 3.6 Potentiostatic polarization test

Figure 11 shows the  $i-t$  response of SLMed 718 and R 718 alloys in 0.05 mol/L  $\text{H}_2\text{SO}_4$  solution under potentiostatic polarization conditions. The inset figure in Fig. 11(a) shows that the stable state current densities ( $i_{ss}$ ) of both alloys are  $2.17 \times 10^{-7} \text{ A}\cdot\text{cm}^{-2}$  and  $3.12 \times 10^{-7} \text{ A}\cdot\text{cm}^{-2}$ , respectively. The lower  $i_{ss}$  of SLMed 718 alloy indicates an enhanced protective capability of the film, due to the greater transfer resistance that hinders species

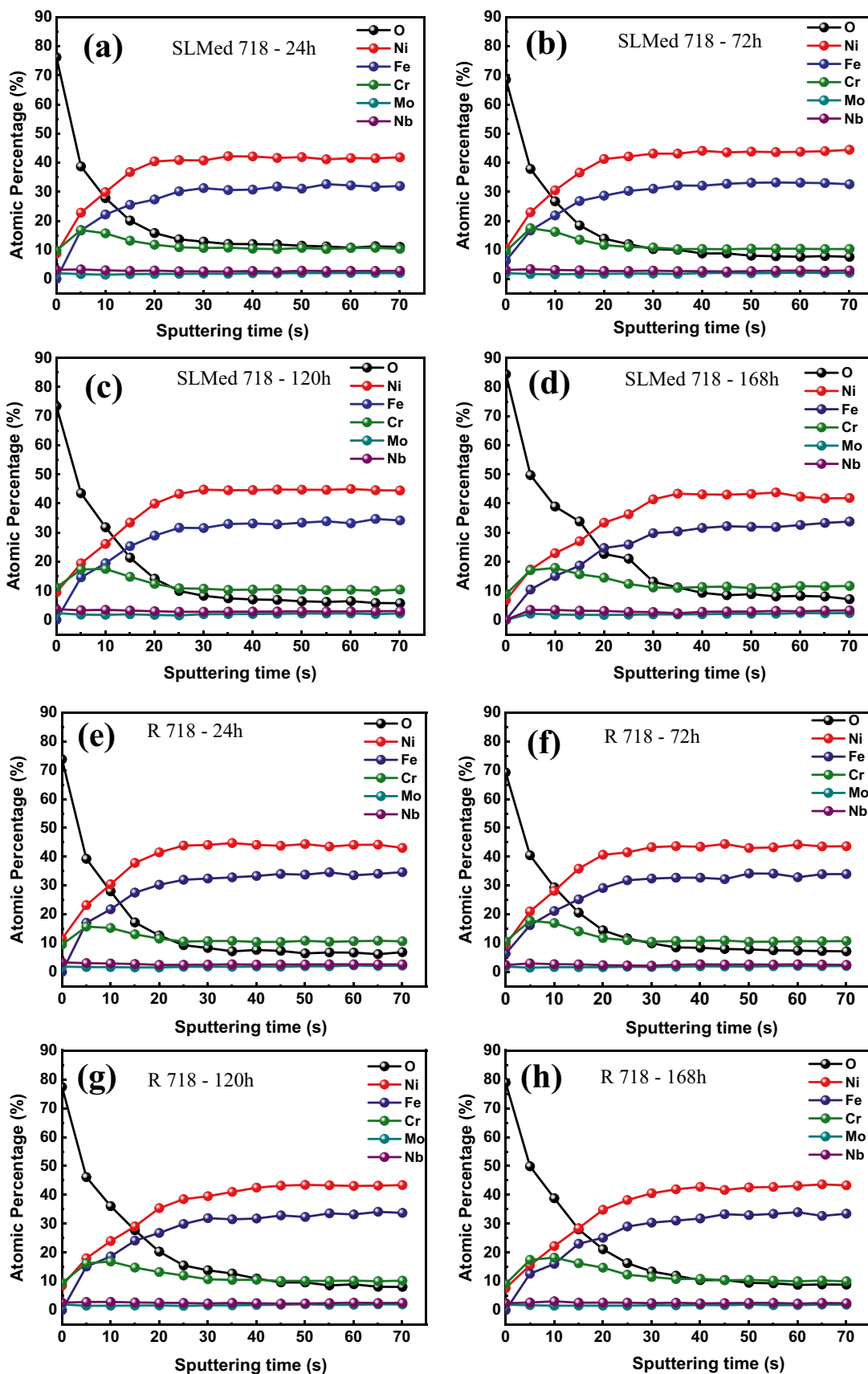


Fig. 9 Depth distribution of element in passive film formed on SLMed 718 alloy (a), (b), (c), (d) and R 718 alloy (e), (f), (g), (h)

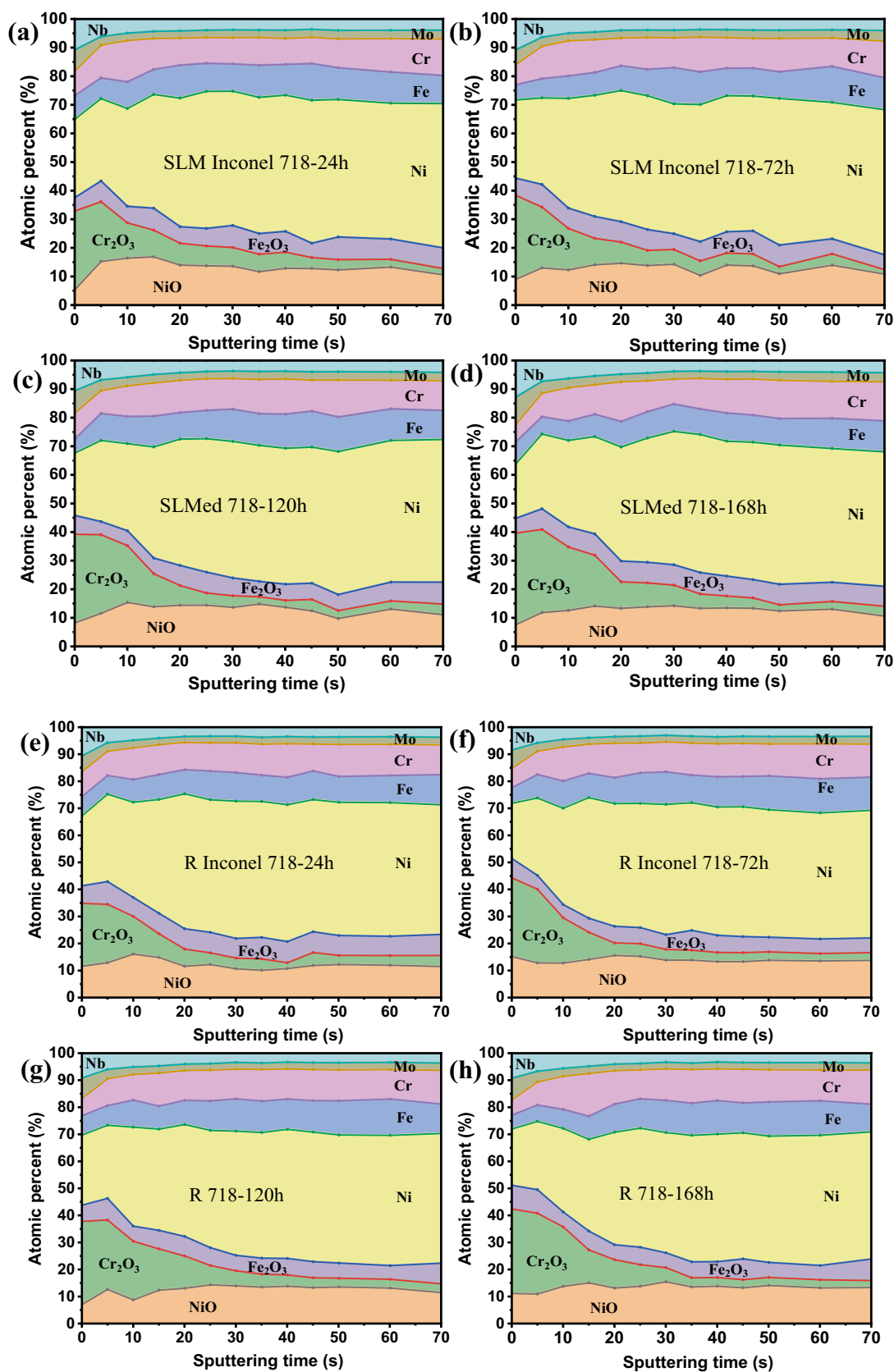
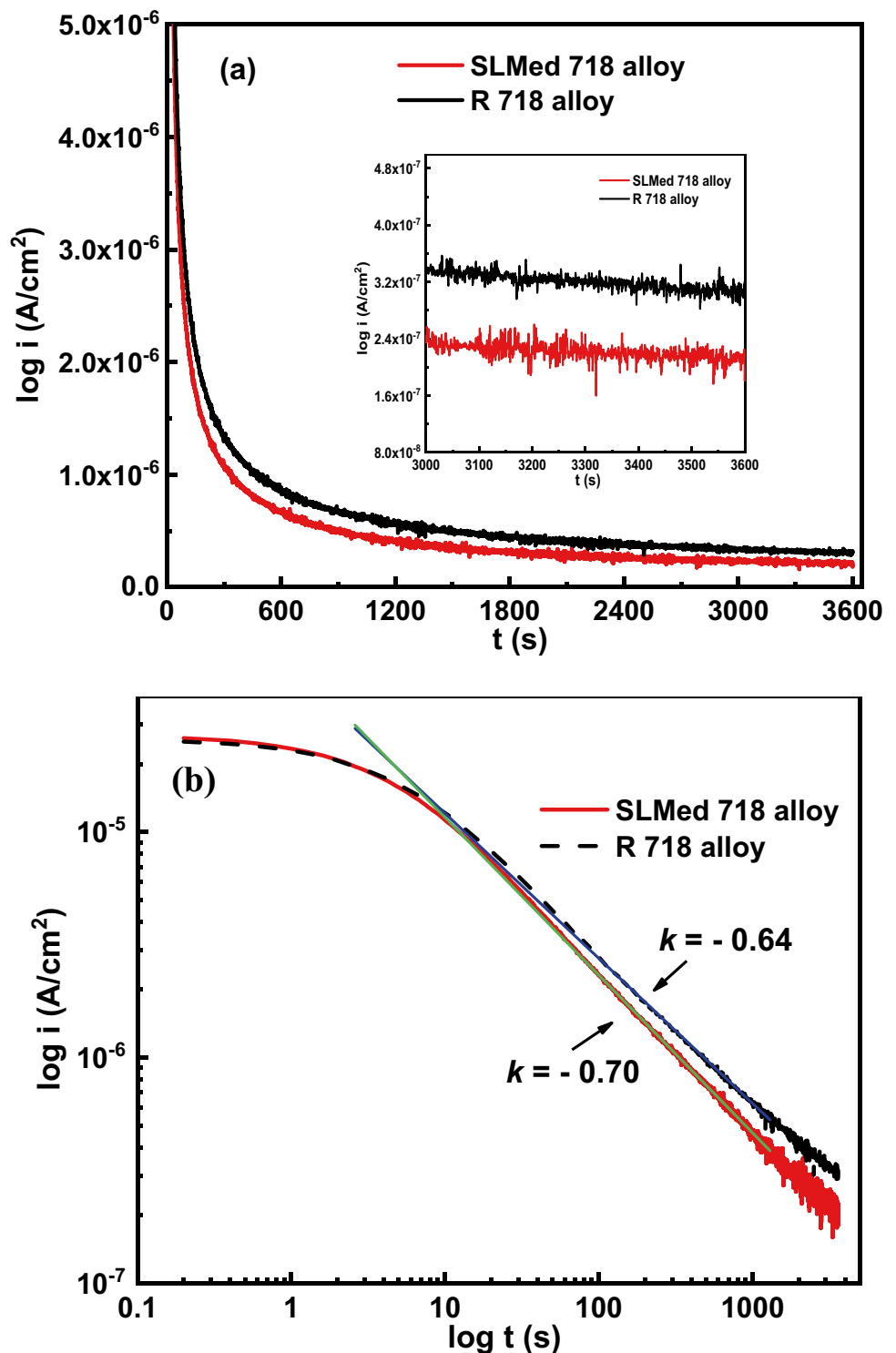


Fig. 10 Depth distribution of different compositions in the passive film for SLMed 718 alloy (a), (b), (c), (d) and R 718 alloy (e), (f), (g), (h)

**Fig. 11**  $i$ - $t$  curves (a) and  $\log i$  -  $\log t$  (b) plots of SLMed 718 and R 718 alloys in 0.05 mol/L  $H_2SO_4$  solution



transportation across the film. In Fig. 11(b), when the polarization time is less than 10 s, the near coincidence of the two curves evidently suggests that the electrochemical response of the two alloys is almost identical. There is a linear relationship of  $\log i$  -  $\log t$  when the polarization time is longer than 10 s. The film growth rate can be

obtained by the slope ( $k$ ) of the descending line segment of the  $\log i$  -  $\log t$  curve [60, 61]. The lower  $k$  values of SLMed 718 alloy indicate the higher film growth rate and the superior protective properties of the film [26], which is consistent with the XPS analysis. As a result, the corrosion resistance of the R 718 alloy was improved.



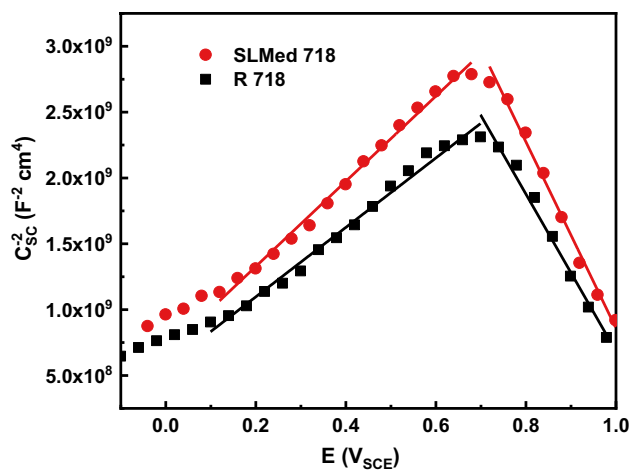


**Fig. 12**  $C_{SC}^{-2}$  vs.  $E$  curves of SLMed and R 718 alloys in 0.05 mol/L  $H_2SO_4$  solution

### 3.7 Mott-Schottky analysis

The space-charge capacitance of an n-type and p-type semiconductor can be given by Eqs. 5 and 6 [51]:

$$\frac{1}{C^2} = \frac{2}{\epsilon \epsilon_0 e N_D} \left( E - E_{FB} - \frac{kT}{e} \right) \quad (5)$$

$$\frac{1}{C^2} = - \frac{2}{\epsilon \epsilon_0 e N_A} \left( E - E_{FB} - \frac{kT}{e} \right) \quad (6)$$

where  $e$  is electron charge ( $1.60 \times 10^{-19}$  C),  $N_D/N_A$  is the donor/acceptor density in the passive film,  $k$  is Boltzmann constant ( $1.38 \times 10^{-23}$  J·mol $^{-1}$ ·K $^{-1}$ ),  $T$  is temperature (K), and  $E$  is the applied potential and  $E_{FB}$  is the flat band potential.

Figure 12 presents  $C_{SC}^{-2}$  vs.  $E$  plots of passive films formed on both SLMed 718 and R 718 alloys. The two regions with positive and negative slope characterized by different capacitance behavior. The same phenomenon was observed in Fe–Cr alloys, stainless steels and CoCrFeMnNi high-entropy alloys [62–64]. When the applied potential is below 0.7 V $_{SCE}$ , the slope of the curves is negative, corresponding to the p-type semiconductivity of the chromium inner oxide layer. In contrary, the region of  $E > 0.7$  V $_{SCE}$  corresponds to the outer layer of the film, which is primarily composed of  $Fe_3O_4$  and/or  $Fe_2O_3$ , behaving as an n-type semiconductor. The difference in the  $C_{SC}^{-2}$  vs.  $E$  plots is related to the thickness of the electron depletion layer or the number of carriers of the charge [62]. Therefore, the acceptor density ( $N_a$ ) and donor density ( $N_d$ ) of SLMed 718 and R 718 alloys can be calculated by the slope of the linear region in the Mott-Schottky curve. The values of  $N_d$  and  $N_a$  for both SLMed 718 and R 718 alloys reach the order of  $10^{21}$  cm $^{-3}$ , which is consistent with the results obtained by Liu

et al. [65]. The  $N_d$  and  $N_a$  of the SLMed Inconel 718 alloy passivation film are  $5.97 \times 10^{21}$  cm $^{-3}$  and  $3.24 \times 10^{21}$  cm $^{-3}$ , respectively. Meanwhile, the  $N_d$  and  $N_a$  of the R 718 alloy passivation film are  $7.16 \times 10^{21}$  cm $^{-3}$  and  $4.05 \times 10^{21}$  cm $^{-3}$ , respectively. The donor density  $N_d$  and the acceptor density  $N_a$  of SLMed 718 alloy are relatively lower compared with those of R 718 alloy. The lower  $N_d$  and  $N_a$  inhibit the migration of ions, which can inhibit the electrochemical/chemical reactions in the passivation film in turn. The lower the carrier density, the more difficulty the ions to diffuse in the passive film. Therefore, the corrosion resistance of SLMed 718 alloy in 0.05 mol/L  $H_2SO_4$  solution is superior to that of R Inconel 718 alloy.

## 4 Conclusions

In this work, the microstructure and electrochemical behaviors of SLMed 718 alloy were systematically investigated and compared with the commercial rolled counterpart. SLMed 718 exhibits superior corrosion resistance with lower corrosion current density and passive current density compared with rolled counterpart. Stable and compact passive films form on the surface of both alloys during immersion test, and their corrosion resistance and protective ability become stronger as immersion time increases. The passive film of SLMed718 alloy is composed of NiO,  $Fe_2O_3$  and  $Cr_2O_3$ . It thickens gradually, and meanwhile, the  $Cr_2O_3$  content increases while the porous NiO content decreases with increasing immersion time, resulting in the enhanced protective ability. In addition, the passive film gradually thickened with time, which exhibited the better protective properties due to less porous NiO and more compact  $Cr_2O_3$ . The significance of this study lied in revealing the advantages of SLMed 718 alloy in terms of corrosion resistance, and providing a foundation for in-depth understanding of its electrochemical behavior and the formation mechanism of surface passive films. Furthermore, the results of this study could guide material design and engineering applications, such as developing more corrosion-resistant materials to extend service life and improve performance in corrosive environment.

**Author contribution** Yanxin Qiao supervised the project; Wentao Zhang and Xinwang shen: material preparation and characterization analysis; Xinwang Shen and Yanxin Qiao designed the experiments; Wentao Zhang, Taghrid S. Alomar and Wen Liu: data plotting and scientific drawing; Yanxin Qiao, Najla AlMasoud and Hassan Algadi: review and editing and supervision; Shunli Zheng, Mohamed H. Helal, Zeinhom M. El-Bahy and Mohamed M. Ibrahim: resources, writing—review and editing, and data curation. All authors discussed experiments and results. All authors have given approval for the final version of the manuscript.

**Funding** We express our gratitude to the financial support of the National Natural Science Foundation of China (Nos. 52001142 and 51975263), the financial support from Princess Nourah bint Abdulrahman University Researchers Supporting Project number (PNURSP2023R18), Princess Nourah bint Abdulrahman University, Riyadh, Saudi Arabia.

**Data availability** The data that support the findings of this study are available from the corresponding author upon reasonable request.

## Declarations

**Competing interests** The authors declare no competing interests.

## References

- Zhao YH, Liu KX, Zhang HB, Tian XL, Jiang QL, Murugadoss V, Hou H (2022) Dislocation motion in plastic deformation of nano polycrystalline metal materials: a phase field crystal method study. *Adv Compos Hybrid Mater* 5:2546–2556
- Zhao YH (2023) Understanding and design of metallic alloys guided by phase-field simulations. *npj Comput Mater* 9:94
- Chen LQ, Zhao YH (2022) From classical thermodynamics to phase-field method. *Prog Mater Sci* 124:100868
- Xin TZ, Tang S, Ji F, Cui LQ, He BB, Lin X, Tian XL, Hou H, Zhao YH, Ferry M (2022) Phase transformations in an ultra-light BCC Mg alloy during anisothermal ageing. *Acta Mater* 239:118248
- Zhao YH, Zhang B, Hou H, Chen WP, Wang M (2019) Phase-field simulation for the evolution of solid/liquid interface front in directional solidification process. *J Mater Sci Technol* 35:1044–1052
- Kuang WW, Wang HF, Li X, Zhang JB, Zhou Q, Zhao YH (2018) Application of the thermodynamic extremal principle to diffusion-controlled phase transformations in Fe-C-X alloys: Modeling and applications. *Acta Mater* 159:16–30
- Zhao Y, Liu K, Hou H, Chen LQ (2022) Role of interfacial energy anisotropy in dendrite orientation in Al-Zn alloys: A phase field study. *Mater Des* 216:110555
- Zhang K, Liu XY, Bi JJ, BaQais A, Xu BB, Amin MA, Hou Y, Liu XL, Li HD, Algadi H, Xu J, Guo ZH (2023) Bimetallic NiCe/Lay catalysts facilitated co-pyrolysis of oleic acid and methanol for efficiently preparing anaerobic hydrocarbon fuels. *New J Chem* 47:18272–18284
- Ruan JC, Chang ZX, Rong HW, Alomar TS, Zhu DP, AlMasoud N, Liao YJ, Zhao RZ, Zhao XY, Li YX (2023) High-conductivity nickel shells encapsulated wood-derived porous carbon for improved electromagnetic interference shielding. *Carbon* 213:118208
- Xin TZ, Zhao YH, Mahjoub R, Jiang JX, Yadav A, Nomoto K, Niu RM, Tang S, Ji F, Quadir Z, Miskovic D, Daniels J, Xu WQ, Liao XZ, Chen LQ, Hagihara K, Li XY, Ringer S, Ferry M (2021) Ultrahigh specific strength in a magnesium alloy strengthened by spinodal decomposition. *Sci Adv* 7:eabf3039
- Liu W, Zhao YH, Zhang YT, Shuai C, Chen LW, Huang ZQ, Hou H (2023) Deformation-induced dynamic precipitation of 14H-LPSO structure and its effect on dynamic recrystallization in hot-extruded Mg-Y-Zn alloys. *Int J Plasticity* 164:103573
- Zhang JB, Wang HF, Kuang WW, Zhang YC, Li S, Zhao YH, Herlach DM (2018) Rapid solidification of non-stoichiometric intermetallic compounds: Modeling and experimental verification. *Acta Mater* 148:86–99
- Tian XL, Zhao YH, Gu T, Guo YL, Xu FQ, Hou H (2022) Cooperative effect of strength and ductility processed by thermomechanical treatment for Cu–Al–Ni alloy. *Mater Sci Eng A* 849:143485
- Tong YG, Wang L, Wang B, Hu YL, Cai ZH, Ren JN, Liu J, Li S (2022) Microstructure and mechanical behavior of carbon fiber reinforced carbon, silicon carbide, and copper alloy hybrid composite fabricated by Cu-Si alloy melt infiltration. *Adv Compos Hybrid Mater* 6:25
- Amrita AM, Ramesh CP (2022) Biodegradable filament for 3D printing process: a review. *Eng Sci* 18:11–19
- Rashkovets M, Nikulina A, Turichin G, Klimova-Korsmik O, Sklyar M (2018) Microstructure and phase composition of ni-based alloy obtained by high-speed direct laser deposition. *J Mater Eng Perform* 27:6398–6406
- Wang HT, Feng W, Liu D, Zhang GD, Liu Y, Wang J, Zou L (2023) Iron-based soft magnetic materials fabricated by laser additive manufacturing. *Eng Sci* 22:809
- Jing YT, Wang RJ, Wang QL, Xiang ZY, Li ZX, Gu HB, Wang XF (2021) An overview of surface-enhanced Raman scattering substrates by pulsed laser deposition technique: fundamentals and applications. *Adv Compos Hybrid Mater* 4:885–905
- Yamanaka K, Shiratori H, Mori M, Omura K, Fujieda T, Kuwabara K, Chiba A (2020) Corrosion mechanism of an equimolar AlCoCrFeNi high-entropy alloy additively manufactured by electron beam melting. *npj Mater Degrad* 4:24
- Pütz RD, Pratesa Y, Oster L, Sharma R, Reisgen U, Zander D (2021) Microstructure and corrosion behavior of functionally graded wire arc additive manufactured steel combinations. *Steel Res Int* 92:2100387
- Costa MM, Dantas TA, Bartolomeu F, Alves N, Silva FS, Miranda G, Toptan F (2019) Corrosion behaviour of PEEK or  $\beta$ -TCP-impregnated Ti6Al4V SLM structures targeting biomedical applications. *T Nonferr Metal Soc* 29:2523–2533
- Wang XL, Liu Z, Wang H, Zeng CC (2023) Direct 3D Printing of piezoelectrets: process feasibility, prototypes fabrication and device performance. *Eng Sci* 21:800
- Yang JM, Zhou B, Han DX, Cui NX, Li B, Shen J, Zhang ZH, Du A (2022) High-precision three-dimensional printing in a flexible, low-cost and versatile way: a review. *ES Mater Manuf* 15:1–13
- Kong DC, Dong CF, Ni XQ, Li XG (2019) Corrosion of metallic materials fabricated by selective laser melting. *npj Mater Degrad* 3:24
- Zhang LN, Ojo OA (2020) Corrosion behavior of wire arc additive manufactured Inconel 718 superalloy. *J Alloy Compd* 829:154455
- Gai X, Bai Y, Li J, Li S, Hou W, Hao Y, Misra RDK (2018) Electrochemical behaviour of passive film formed on the surface of Ti-6Al-4V alloys fabricated by electron beam melting. *Corros Sci* 145:80–89
- Kong DC, Dong CF, Ni XQ, Zhang L, Luo H, Li RX, Li XG (2020) The passivity of selective laser melted 316L stainless steel. *Appl Surf Sci* 504:144495
- Qian CH, Xu HZ, Zhong Q (2020) The influence of process parameters on corrosion behavior of Ti6Al4V alloy processed by selective laser melting. *J Laser Appl* 32:032010
- Bai Y, Gai X, Li SJ, Zhang LC, Liu YJ, Hao YL, Gao YB (2017) Improved corrosion behaviour of electron beam melted Ti-6Al-4V alloy in phosphate buffered saline. *Corros Sci* 123:289–296
- Dai NW, Zhang LC, Zhang JX, Chen QM, Wu ML (2016) Corrosion behavior of selective laser melted Ti-6Al-4V alloy in NaCl solution. *Corros Sci* 102:484–489
- Guo PF, Lin X, Xu JJ, Li JQ, Liu JR, Huang WD (2017) Electrochemical removal of different phases from laser solid formed Inconel 718. *J Electrochem Soc* 164:E151–E157
- Tang YB, Shen XW, Liu ZH, Qiao YX, Yang LL, Lu DH, Zou JS, Xu J (2022) Corrosion behaviors of selective laser melted inconel 718 alloy in NaOH solution. *Acta Metall Sin* 58:324–333
- Tang YB, Shen XW, Qiao YX, Yang LL, Chen J, Lu DH, Zhang ZY (2021) Corrosion behavior of a selective laser melted inconel 718 alloy in a 3.5 wt.% NaCl solution. *J Mater Eng Perform* 30:5506–5514

34. Du DF, Dong AP, Shu D, Zhu GL, Sun BD, Li X, Lavernia E (2019) Influence of build orientation on microstructure, mechanical and corrosion behavior of Inconel 718 processed by selective laser melting. *Mater Sci Eng A* 760:469–480
35. Guo PF, Lin X, Liu JR, Xu JJ, Li JQ, Zhang YF, Huang WD (2020) Passive behavior of nickel-based superalloys prepared by high-deposition-rate laser solid forming additive manufacturing. *Corros Sci* 177:109036
36. Lu FY, Wan HY, Ren X, Huang LM, Liu HL, Yi X (2022) Mechanical and microstructural characterization of additive manufactured Inconel 718 alloy by selective laser melting and laser metal deposition. *J Iron Steel Res Int* 29:1322–1333
37. Zhang MH, Zhang BC, Wen YJ, Qu XH (2022) Research progress on selective laser melting processing for nickel-based superalloy. *Int J Miner Metall Mater* 29:369–388
38. Luo H, Gao SJ, Dong CF, Li XG (2014) Characterization of electrochemical and passive behaviour of Alloy 59 in acid solution. *Electrochim Acta* 135:412–419
39. Zagidulin D, Zhang XR, Zhou JG, Noël JJ, Shoesmith DW (2013) Characterization of surface composition on Alloy 22 in neutral chloride solutions. *Surf Interface Anal* 45:1014–1019
40. Qiao YX, Zheng ZB, Yang HK, Long J, Han PX (2023) Recent progress in microstructural evolution, mechanical and corrosion properties of medium-Mn steel. *J Iron Steel Res Int* 30:1463–1476
41. Shang XL, Wang ZJ, Wu QF, Wang JC, Li JJ, Yu JK (2018) Effect of Mo addition on corrosion behavior of high-entropy alloys CoCrFeNiMox in aqueous environments. *Acta Metall Sin (Engl Lett)* 32:41–51
42. Liu XB, Xiao WJ, Song LJ, Xiao H (2022) Solidification structure and aging response of laser additive manufactured Inconel 718. *Appl Phys A* 128:516
43. Luo GY, Cheng MP, Zhao LZ, Tang YC, Yao JH, Cui HL, Song LJ (2021) Preferential interdendritic oxidation of laser additively manufactured Inconel 718. *Corros Sci* 179:109144
44. Luo SC, Huang WP, Yang HH, Yang JJ, Wang ZM, Zeng XY (2019) Microstructural evolution and corrosion behaviors of Inconel 718 alloy produced by selective laser melting following different heat treatments. *Addit Manuf* 30:100875
45. You XG, Tan Y, Zhao LH, You QF, Wang YN, Ye F, Li JY (2018) Effect of solution heat treatment on microstructure and electrochemical behavior of electron beam smelted Inconel 718 superalloy. *J Alloy Compd* 741:792–803
46. Chen T, John H, Xu J, Lu QH, Hawk J, Liu XB (2013) Influence of surface modifications on pitting corrosion behavior of nickel-base alloy 718. Part 1: Effect of machine hammer peening. *Corros Sci* 77:230–245
47. Li L, Qiao YX, Zhang LM, Li CT, Liu Z, Ma RY, Yang LL, Li JY, Zheng YG (2023) Effects of cavitation erosion-induced surface damage on the corrosion behaviour of TA31 Ti alloy. *Ultrason Sonochem* 98:106498
48. Lv JL, Luo HY (2013) Comparison of corrosion properties of passive films formed on phase reversion induced nano/ultrafine-grained 321 stainless steel. *Appl Surf Sci* 280:124–131
49. Wang ZB, Hu HX, Zheng YG (2018) Synergistic effects of fluoride and chloride on general corrosion behavior of AISI 316 stainless steel and pure titanium in H<sub>2</sub>SO<sub>4</sub> solutions. *Corros Sci* 130:203–217
50. Zhao Y, Xiong H, Li XP, Qi WL, Wang JD, Hua Y, Zhang T, Wang FH (2021) Improved corrosion performance of selective laser melted stainless steel 316L in deep sea environment. *Corros Commun* 2:55–62
51. Qiao YX, Wang XY, Yang LL, Wang XJ, Chen J, Wang ZB, Zhou HL, Zou JS, Wang FH (2022) Effect of aging treatment on microstructure and corrosion behavior of a Fe–18Cr–15Mn–0.66N stainless steel. *J Mater Sci Technol* 107:197–206
52. Chen JJ, Xiao Q, Lee HB, Jeong CW, Jang KN, Jang CH (2022) Enhanced pitting resistance of directed energy deposition 316L stainless steel by post-manufacturing heat treatment. *npj Mater Degrad* 6:33
53. Gao FY, Qiao YX, Chen J, Yang LL, Zhou HL, Zheng ZB, Zhang LM (2023) Effect of nitrogen content on corrosion behavior of high nitrogen austenitic stainless steel. *npj Mater Degrad* 7:75
54. Wang WR, Qi W, Zhang XL, Yang X, Xie L, Li DY, Xiang YH (2021) Superior corrosion resistance-dependent laser energy density in (CoCrFeNi)<sub>95</sub>Nb<sub>5</sub> high entropy alloy coating fabricated by laser cladding. *Int J Miner Metall Mater* 28:888–897
55. Hirschorn B, Orazem ME, Tribollet B, Vivier V, Frateur I, Musiani M (2010) Determination of effective capacitance and film thickness from constant-phase-element parameters. *Electrochim Acta* 55:6218–6227
56. Bakare MS, Voisey KT, Roe MJ, McCartney DG (2010) X-ray photoelectron spectroscopy study of the passive films formed on thermally sprayed and wrought Inconel 625. *Appl Surf Sci* 257:786–794
57. Liu WL, Wang QY, Hao J, Zou GN, Zhang P, Wang GW, Ai ZY, Chen HD, Ma H, Song D (2023) Corrosion resistance and corrosion interface characteristics of Cr-alloyed rebar based on accelerated corrosion testing with impressed current. *J Mater Res Technol* 22:2996–3009
58. Cui ZY, Chen SS, Dou YP, Han SK, Wang LW, Man C, Wang X, Chen SG, Cheng YF, Li XG (2019) Passivation behavior and surface chemistry of 2507 super duplex stainless steel in artificial seawater: Influence of dissolved oxygen and pH. *Corros Sci* 150:218–234
59. Lv JL, Luo HY (2012) Electrochemical investigation of passive film in pre-deformation AISI 304 stainless steels. *Appl Surf Sci* 263:29–37
60. Nelson JC, Oriani RA (1990) Current transients caused by potential jumps applied to passivating films on nickel. *Electrochim Acta* 35:1719–1726
61. Li L, Qiao YX, Zhang LM, Ma AL, Daniel EF, Ma RY, Chen J, Zheng YG (2023) Effect of cavitation erosion induced surface damage on pitting and passive behaviors of 304L stainless steel. *Int J Miner Metall Mater* 30:1338–1352
62. Ningshen S, Kamachi Mudali U, Mittal VK, Khatak HS (2007) Semiconducting and passive film properties of nitrogen-containing type 316LN stainless steels. *Corros Sci* 49:481–496
63. Taveira LV, Montemor MF, Da Cunha BM, Ferreira MG, Dick LFP (2010) Influence of incorporated Mo and Nb on the Mott-Schottky behaviour of anodic films formed on AISI 304L. *Corros Sci* 52:2813–2818
64. Luo H, Zou S, Chen YH, Li Z, Du CW, Li XG (2020) Influence of carbon on the corrosion behaviour of interstitial equiatomic CoCrFeMnNi high-entropy alloys in a chlorinated concrete solution. *Corros Sci* 163:108287
65. Liu L, Li Y, Wang FH (2007) Influence of nanocrystallization on passive behavior of Ni-based superalloy in acidic solutions. *Electrochim Acta* 52:2392–2400

**Publisher's Note** Springer Nature remains neutral with regard to jurisdictional claims in published maps and institutional affiliations.

Springer Nature or its licensor (e.g. a society or other partner) holds exclusive rights to this article under a publishing agreement with the author(s) or other rightsholder(s); author self-archiving of the accepted manuscript version of this article is solely governed by the terms of such publishing agreement and applicable law.